Frequency Domain Electromagnetic Sensor Array Development

Final Report

SERDP SEED Project MM-1450

September 17, 2007

Principal Investigator: David J. Wright

SAIC, Advanced Sensors and Analysis Division
120 Quade Drive
Cary, NC 27513

Abstract

A laboratory prototype frequency domain electromagnetic induction sensor array suitable for simultaneous operation with an array of cesium vapor total field magnetometers has been designed and fabricated and has undergone limited bench testing. The design is based on the GEM-3 active primary field cancellation technology, which creates a "magnetic cavity" for each receive coil in the array. The array's magnetometers would be mounted inside the receive coils, within the magnetic cavities. This is very important because the primary transmit field would otherwise be strong enough to shift the total magnetic field vector (static magnetic field plus EMI components) outside the operating envelope of the magnetometers. Because the array configuration does not have the symmetry of a standard GEM-3, in-phase drift tends to be more severe. Tests with the prototype array show drift rates roughly one order of magnitude larger than with a standard GEM-3. However, demedian filtering such as that used for the MM-0033 towed GEM-3 array can correct for the drift. The most serious issue for the array is structural rigidity. When the array is bent, the bucking coils do not properly cancel the field from the outer transmit loop. Calculations indicate that bucking errors amounting 10's of ppm can be caused by bending the array by a few tenths of a degree over a distance of about 30 cm. The array would have to be held stiff to this sort of tolerance. For towed applications on land this may be difficult because the array will be subjected to significant bending stresses as it is towed over any realistic terrain. The bouncing and jostling motions for vehicle towed systems tend to have scales comparable to those of buried UXO signals. The situation may not be so serious for marine applications where the array would be buoyed up and not subject to such severe stresses.

Contents

Figures

Tables

Acronyms

AC	Alternating Current (time varying)
ADC	Analog-to-Digital Converter
ATV	All-Terrain Vehicle
CW	Continuous Wave
DC	Direct Current (constant in time)
EM	Electromagnetic
EMI	Electromagnetic Induction
ENOB	Effective Number of Bits (for analog-to-digital conversion)
EQT	Environmental Quality Technology
FDEM	Frequency Domain Electromagnetic
MTADS	Multisensor Towed Array Detection System
ppm	Parts per million (of the unbucked primary transmit field at the receiver coil)
TDEM	Time Domain Electromagnetic
TMF	Total Magnetic Field
UXO	Unexploded Ordnance

1. Introduction

Digital geophysical mapping applied to the detection of buried unexploded ordnance (UXO) entails electromagnetic induction (EMI) and/or total magnetic field (TMF) surveys of the UXO-contaminated site. Arrays of TMF and EMI sensors are complementary, and it was found in the Jefferson Proving Ground Technology Demonstration Program that demonstrators who used a combination of EMI and magnetometry based sensors provided the best UXO detection performance [1]. Significant cost savings from improved detection efficiency can be realized through simultaneous deployment of both technologies. Many sites also present unique challenges to deployment and precise positioning of geophysical instrumentation. These difficulties result in increased costs for any given survey deployment as well as a diminished precision in the spatial correlation of data collected in subsequent passes or re-surveys. Diminished sensor location precision makes it difficult to correlate targets selected from separately collected data sets. It also has a serious detrimental effect on the ability to distinguish UXO from ordnance scrap when applying physics-based analysis algorithms. EMI and magnetometer arrays deployed simultaneously may provide the relative positioning precision required to support these analyses.

The standard cesium vapor total field magnetometer (e.g. Geometrics G822A) is severely influenced by low frequency (<200 Hz) fields that have a significant component aligned with the geomagnetic field. Time-domain EMI sensors such as the EM61 radiate considerable power at low frequencies, and cause serious interference with magnetometers of this sort. The top plot in Figure 1 illustrates the problem. As shown in the inset photograph, we set up a G822A magnetometer ~45 cm above and ~25 cm laterally offset from the primary coil of a Geonics EM61-HH pulsed EMI sensor. The magnetometer is sampled at 100 Hz. With the EM61-HH running (red curve), the TMF is offset from the geomagnetic field value (blue curve) by about 10,000 nT and has quasi-periodic noise fluctuations with an amplitude of several thousand nT. If the EM61-HH is carefully maneuvered around beneath the magnetometer, the noise can be reduced to tens of nT. This corresponds to a configuration in which the primary field of the EMI sensor is orthogonal to the geomagnetic field at the magnetometer. If the EMI fields are not too strong, the problem can be avoided by interleaving the magnetometer operation with the EMI sensor's transmitter pulse sequence [2, 3] The engineering details for application to single sensor and towed array configurations have been worked out in ESTCP projects MM-0208, -0414 and -0531. CW frequency domain EMI systems do not cause this type of interference. Provided that the frequency is above about 200 Hz and is more than 200 Hz away from the Larmor frequency (~150 kHz), the primary field from a frequency domain EMI sensor broadens the spectral line of the magnetometer, but does not directly introduce fluctuating noise in the magnetic field measurements. The bottom plot in Figure 1 shows data collected with the 822A with and without a Geonics EM31 frequency domain EMI sensor (9.8 kHz) operating simultaneously. The magnetometer was 14 cm directly above the transmit coil of the EM31 in this test. With the EM31 radiating, the noise level of the magnetic data is indistinguishable from background noise levels (<0.05 nT rms). This in spite of the fact that, at this range, the primary field strength of the EM31 is about six times larger than the primary field strength of the EM61-HH in the data shown in the top plot. Note that the vertical scale range in the top plot is two orders of magnitude larger than the vertical scale range in the bottom plot. The only observable effect of the EM31 is a DC offset which depends on the strength and orientation of the EMI primary field at the magnetometer head.

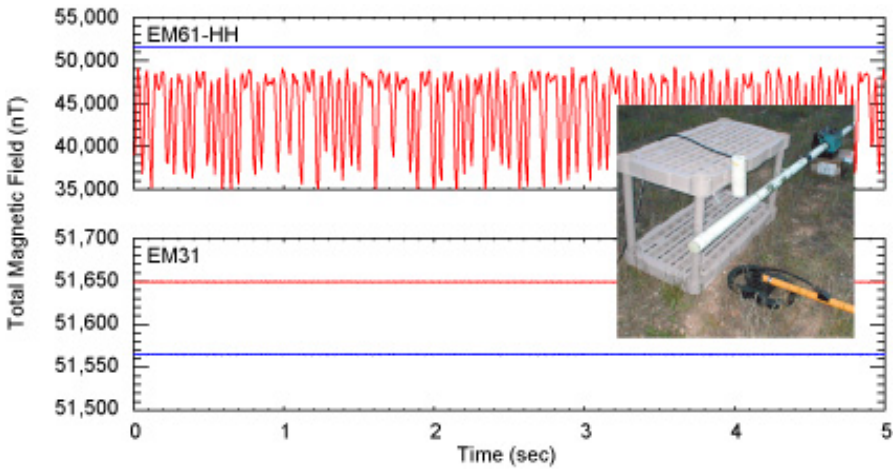

Figure 1. TMF data with (red) and without (blue) EMI sensors operating nearby.

We developed and demonstrated a handheld combined TMF/EMI sensor as part of the Army Environmental Quality Technology (EQT) Program [4, 5]. The sensor, shown in Figure 2, combined a Geometrics Cesium vapor magnetometer (model 823A) with a Geophex GEM-3 frequency-domain EMI sensor operating at three frequencies (3, 6 and 13 kHz). The objective of the project reported on here was an evaluation of the feasibility of extending this technology to array configurations.

The primary technical issue for simultaneous collection of EMI and TMF data is the effect of the EMI primary (transmitted) field on the magnetic field measurement. This is discussed in detail in §2 below. For a continuous wave (CW) EMI sensor, provided that the net magnetic field (geomagnetic plus EMI) lies within the operating envelope of the magnetometers, the component of the EMI field parallel to the geomagnetic field averages to zero, while the perpendicular component is rectified and produces a DC magnetic offset. This can be corrected for by monitoring the sensor orientation relative to the geomagnetic field with a fluxgate magnetometer. Section 3 summarizes the results of the coil configuration design study. The final design is based on the GEM-3 active primary field cancellation technology, which creates a "magnetic cavity" for each receive coil in the array. The array's magnetometers would be mounted inside the receive coils, within the magnetic cavities. This is very important because the primary transmit field would otherwise be strong enough to shift the total magnetic field vector (static magnetic field

Figure 2. Combined TMF/EMI sensor developed for the Army EQT Program.

plus EMI components) outside the operating envelope of the magnetometers. Section 4 describes the prototype sensor mockup and bench testing. Topics addressed in this section include sensor calibration and drift, array flexure, magnetometer placement and target classification and discrimination. The laboratory prototype of the array was constructed for this project by Geophex, Ltd. Because the array configuration does not have the symmetry of a standard GEM-3, in-phase drift tends to be more severe. Tests with the prototype array show drift rates roughly one order of magnitude larger than with a standard GEM-3. However, demedian filtering such as that used for the MM-0033 towed GEM-3 array can correct for the drift. The most serious issue for the array is structural rigidity. When the array is bent, the bucking coils do not properly cancel the field from the outer transmit loop. Calculations indicate that bucking errors amounting 10's of ppm can be caused by bending the array by a few tenths of a degree over a distance of about 30 cm. The array would have to be held stiff to this sort of tolerance. For towed applications on land this may be difficult because the array will be subjected to significant bending stresses as it is towed over any realistic terrain. The bouncing and jostling motions for vehicle towed systems tend to have scales comparable to those of buried UXO signals. The situation may not be so serious for marine applications where the array would be buoyed up and not subject to such severe stresses. The conclusions are summarized in §5.

2. EMI/TMF Interaction

The primary technical issue for simultaneous collection of EMI and total magnetic field data is the effect of the EM transmitted field on the magnetic field measured by the magnetometers. The Cesium vapor magnetometers typically used for digital geophysical mapping can respond to magnetic field fluctuations at frequencies below about 200 Hz. At substantially higher frequencies, they average the magnitude of the field over the fluctuations. A time domain EMI sensor like the Geonics EM61 radiates substantial power at low frequencies, causing serious magnetic interference. At frequencies well above 200 Hz and below the magnetometer Larmor frequency (150 kHz), the primary (transmitted) field of a frequency domain EMI sensor simply produces a DC offset in the magnetometer response. The field vector is the vector sum of the static geomagnetic field and the oscillating primary (transmitted) field of the EMI sensor. The component of the primary field aligned with the geomagnetic field averages out, while that orthogonal to the geomagnetic field gets rectified and adds to the geomagnetic field as follows. Using angle brackets to denote averaging,

$$H_{meas} = < \left| \vec{H}_{earth} + \vec{H}_{emi} \right| > = H_{earth} < \sqrt{(1 + H_{\parallel} / H_{earth})^2 + (H_{\perp} / H_{earth})^2} >$$

where $H_{\parallel}$ is the component of H_{emi} parallel to H_{earth}, and $H_{\perp}$ is the perpendicular component. Assuming that $H_{earth} >> H_{emi}$, we can expend the rightmost term in a Taylor series. Keeping all terms to second order, we have

$$H_{meas} = H_{earth} < 1 + H_{\parallel} / H_{earth} + \tfrac{1}{2} (H_{\perp} / H_{earth})^2 >$$

For a FDEM signal, the linear term averages to zero, while the quadratic term averages to a constant offset which we refer to as the EMI induced heading error. Figure 3 shows the EMI induced heading error as a function of the primary field strength at the magnetometer for two orientations. The blue curve is the expected offset for the case where the angle between the primary field and the geomagnetic field is 25°, which would be the case for a level sensor with the magnetometer positioned along the axis of the transmit coil, assuming a nominal geomagnetic field inclination of 65°. The red curve shows the corresponding "worst case" offset when the primary field is oriented perpendicular to the geomagnetic field.

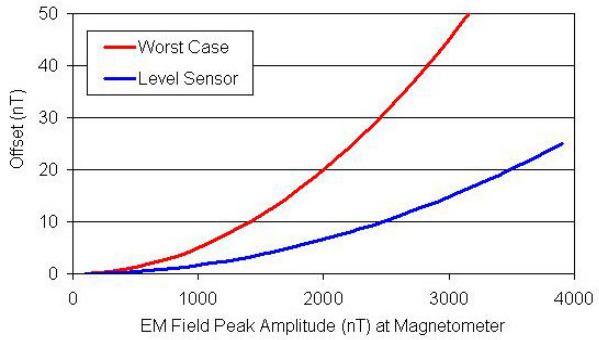

Figure 3. Nominal and worst case EM induced heading errors as a function of primary field strength at the magnetometer.

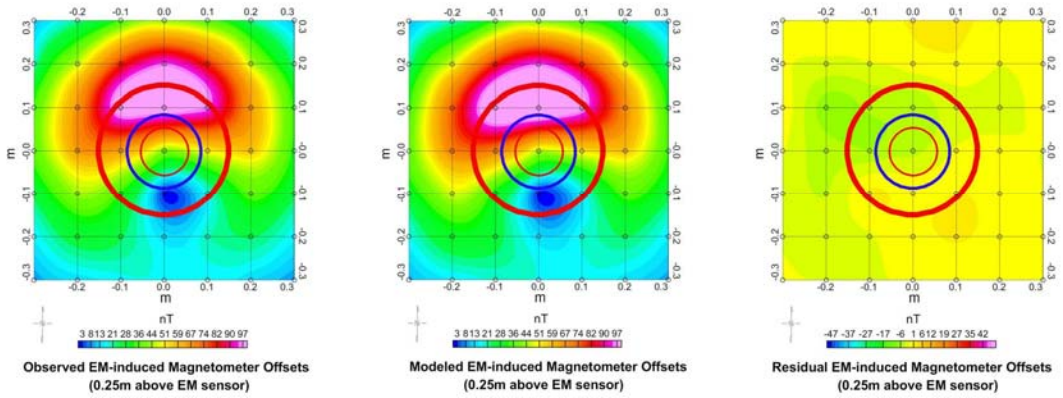

Figure 4. Observed, modeled, and residual EM-induced errors in the measured magnetic data. The EM73 transmit coil positions are shown in red. The asymmetry in the residual error plot occurs near the physical location of the transmit driver interface connection.

Figures 4 and 5 show observed and modeled heading errors induced by the prototype Geonics EM73 FDEM sensor [5], which operates at a frequency of 9.8 kHz and has a net transmit dipole moment of 1.9 amp-m^2. Figure 4 shows heading errors over a horizontal plane 0.25 m above the EM73 coils. The left hand image shows offsets measured while the EM73 was cycled on and off. The concentric circles show the transmit and bucking coils (in red) and the receive coil (in blue). Calculated EMI induced heading errors are plotted in the center panel, and the residual (observed minus modeled) is plotted in the right hand panel. The modeled calculations used a coarse estimate of the total magnetic field vector components based on the IGRF2000 Geomagnetic field model. Figure 5 shows observed and calculated magnetic offsets in the plane of the EM73 coils, offset from the center by 30 cm, as a function of the angle between the primary field vector and the geomagnetic field vector. The offset approaches zero as the angle between the field components approaches zero. The results presented in these figures show that if the sensor orientation relative to the geomagnetic field is monitored, then the EMI induced heading error can be corrected. Since the EMI induced DC field contributions are small compared to the geomagnetic field (~100 nT *vs.* 50,000 nT), this orientation can be easily monitored with a good quality 3-axis fluxgate magnetometer.

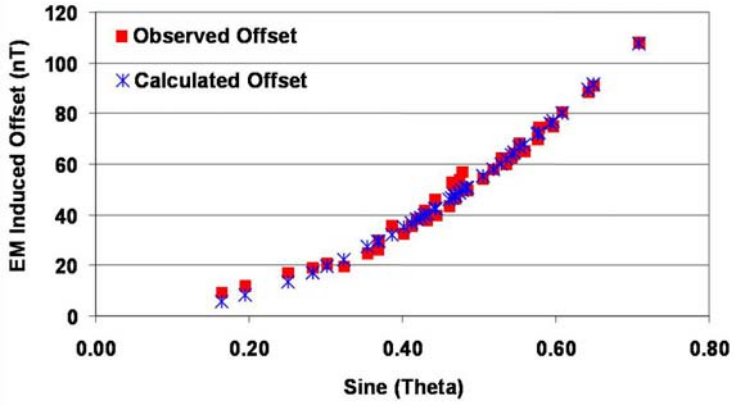

Figure 5. Magnetic offsets vs. angle between primary field and geomagnetic field.

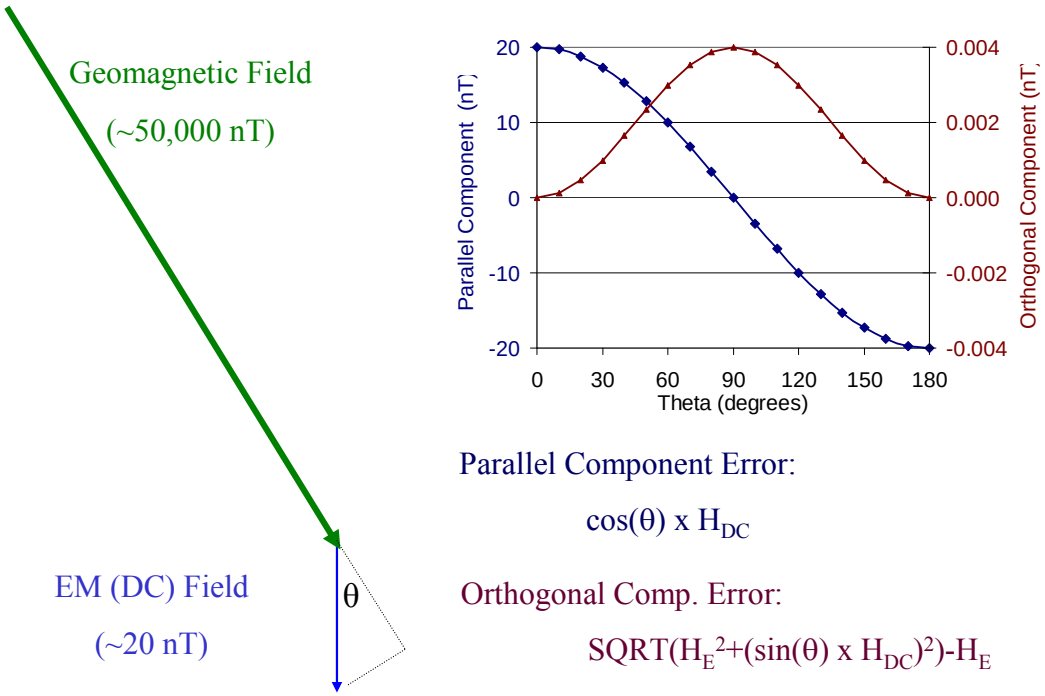

Figure 6. Induced heading errors for DC field components.

The GEM-3 FDEM sensor [6] is similar to the EM73 in that both employ a coplanar concentric coil configuration with active cancellation of the primary field over the area enclosed by the receive coil. However, the GEM-3 uses digital electronics and waveform synthesis, while the EM73 is an analog sensor. For the GEM-3, comparisons between observed and modeled EMI induced heading errors reveal residual heading errors that we believe are caused by small residual DC currents flowing in the GEM-3 transmit coils, probably associated with the digital synthesized waveform which the GEM-3 employs.

The mechanism by which a DC field affects the magnetic field is similar to that of an AC field described above, with some important differences. The component of the DC field that is aligned with the Earth's field will either directly add to or subtract from the Earth's field. For an AC field, this component averages to zero. Fortunately the residual DC field transmitted by the GEM-3 is very small relative to that of the AC field. Because the DC field is so weak, the component of the DC field that is normal to the geomagnetic field has a negligible effect on the total magnetic field. The result is that the DC field can impose a negative or positive offset on the measured total magnetic field, and this offset is maximized when the DC field is aligned with the geomagnetic field (i.e. this effect is orthogonal to that of an AC field). The situation is illustrated schematically in Figure 6. This effect has to be included in compensating for EMI induced heading errors with a digital instrument that has residual DC currents in the coils. The strength of the residual DC currents is not known a priori, but can be determined empirically by fitting the combined AC/DC model to the observed offsets as a function of the orientation of the geomagnetic field. This is illustrated in Figure 7. The setup is similar to that for Figure 5, except that the EMI sensor is a 64 cm GEM-3 operating in multi-frequency mode at 3, 6 and 13 kHz. In this example, the DC offset term is comparable to the AC term.

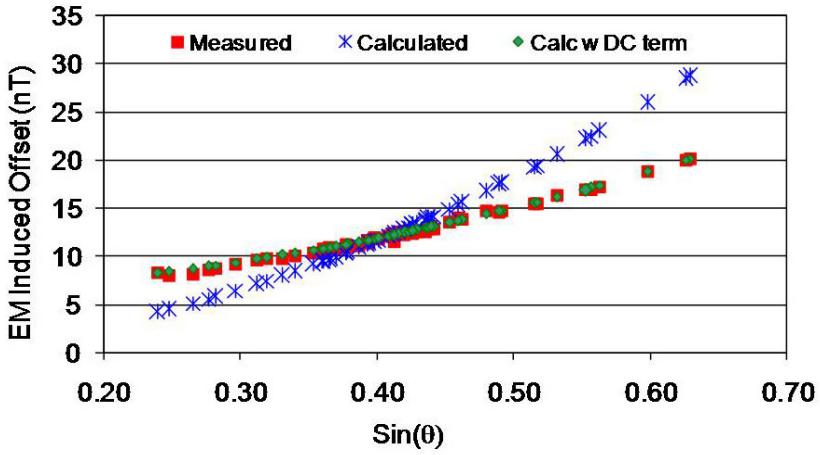

Figure 7. EMI induced offsets with DC correction factor for GEM-3.

3. Coil Configuration Design Study

The key design consideration in this project is the development of a coil configuration that is suitable for deploying an array of CW EMI sensors simultaneously with an array of TMF sensors. The first issue is the choice of an appropriate approach to nulling the primary field contribution to the secondary field measurement by the receive coil. There are three basic approaches: electronic nulling, passive nulling and active nulling.

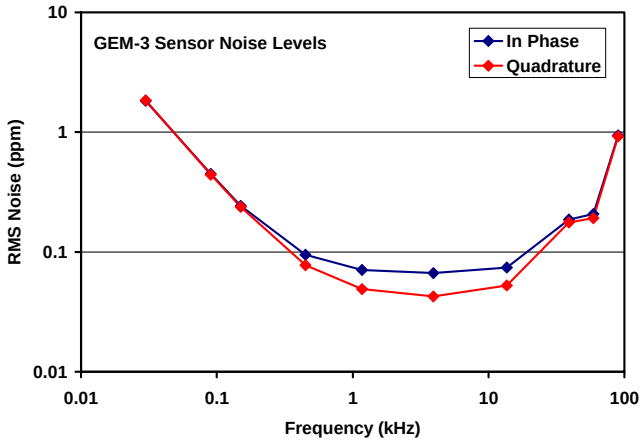

Figure 8. Sensor noise level *vs.* frequency for standard GEM-3.

In its most simple form, electronic nulling involves accurately measuring the combined primary and secondary (induced) fields at the receiver, then estimating and subtracting the prinary field contribution. In order to do successfully accomplish this, the total field must be measured with a high degree of precision. Figure 8 shows measured rms sensor noise as a function of frequency for a standard GEM-3. The units are parts per million (ppm) of the primary transmit field (without bucking) at the Rx coil. As a design goal, we want to be able to measure signals down to this level. There are many commercially available 24-bit analog-to-digital converters (ADCs) that operate at sample rates of 100's of kHz, none with higher resolution. The effective number of bits (ENOB) delivered by these ADCs is limited by internal noise and signal distortion and is actually somewhat less than the specified resolution [7]. Their performance falls short of the 26-bit ADC precision (including the sign bit) that would be needed to resolve the ~0.03 ppm noise floor at mid-frequencies shown in Figure 8.

Passive nulling is implemented by differencing signals from a pair of receive coils that are excited equally by the primary field from the transmit coil, but not by the secondary field due to the target. There are two basic geometries for passive nulling: coplanar and coaxial. Figure 9 shows an EMI sensor arrangement with coplanar passive nulling. This arrangement was used in SERDP project MM-1315 to study various aspects of the time and frequency domain response of UXO items and simple test objects [8]. The basic problem with this arrangement is that differencing the signals from the two coplanar receive coils to null the primary field also reduces the signal from a target below the sensor. This has the effect of increasing the already severe EM signal falloff with target depth from R^{-6} to R^{-7}. The coaxial configuration alleviates this problem to some extent. In the coaxial configuration, the receive coils are displaced vertically, one above

Figure 9. Coplanar passive nulling arrangement used in SERDP project MM-1315.

(reference channel) and one below (signal channel) the transmit coil. The Geophex GEM-5 [9] is an example. The diagram in Figure 10 shows a GEM-5 array configuration with five receive coil pairs and a large transmit loop. The picture on the left shows a GEM-5 array towed behind an ATV. This array is 210 cm wide by 30 cm long by 50 cm tall and contains six receive coil pairs. It has a transmit moment of 180 amp-m^2 at 270 Hz. The magnetic fields due to the primary field transmit coil are extremely large, ~$6.5x10^4$ nT in the plane of the lower receive coils. This is more than strong enough to cause violations of the operating parameters of the magnetometers.

Cesium vapor magnetometers operate properly only if the magnetic field is between 20,000 and 100,000 nT and oriented so that it intersects the longitudinal axis of the magnetometer at 45° ±30° as shown in Figure 11. If the EMI primary field at the magnetometer is strong enough, it will cause the net magnetic vector to violate the operating limits of the magnetometer by exceeding the dynamic range limits or by causing the intersection angle of the vector to fall too close to the magnetometer's longitudinal or lateral axis. In any reasonable deployment mode the orientation of the magnetometer with respect to the Earth's field will be variable, and EMI induced fields with strength comparable to the geomagnetic field are likely to cause voilations of the net field strength and intersection angle limits noted above. The EM array must employ active bucking to create areas where the net EM field is sufficiently reduced that the magnetometer operating parameters are not violated.

The GEM-3 sensor employs active nulling to create a magnetic "cavity" at the location of the receive coil [6], which turns out to be an excellent location for simultaneously operating a magnetometer [4]. The Naval Research Laboratory has developed and demonstrated a towed array of three GEM-3 sensors under ESTCP project MM-0033 [10]. The array is shown in Figure 12. Each of the three sensors is independently nulled by a bucking coil (diameter 53.2 cm, 5 turns) transmitting in opposition to the primary transmit coil (diameter 96 cm, 10 turns). To

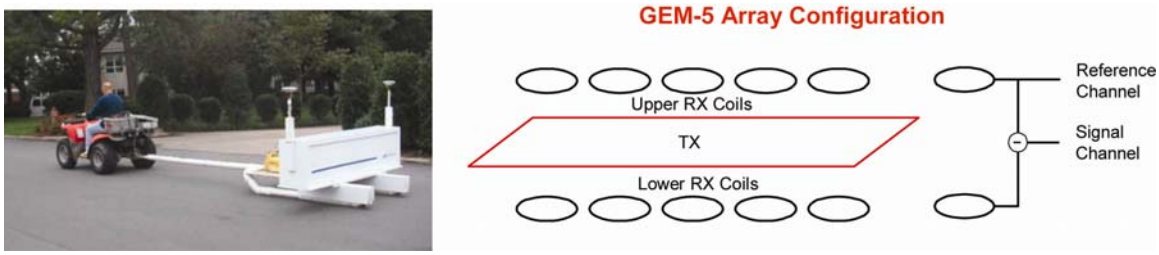

Figure 10. GEM-5 coaxial array configuration.

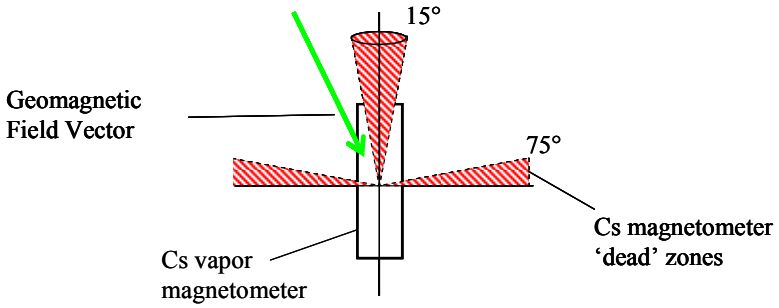

Figure 11. Cesium magnetometer orientation requirements

eliminate cross-talk between the sensors, they are fired sequentially rather than simultaneously. This would create a problem for simultaneous operation with magnetometers because of the low frequency field fluctuations caused by switching the individual sensors on and off. To alleviate this problem, we choose to go with a large transmit coil as in the GEM-5 array, combined with multiple bucking and receive coil pairs. The proposed array configuration is shown in Figure 13. There are five bucking/receive coil pairs inside a 1m long by ½ m wide transmit coil. The bucking coils are shown in red and the receive coils in black. The array accommodates five magnetometers mounted in the magnetic cavities created by the bucking coils

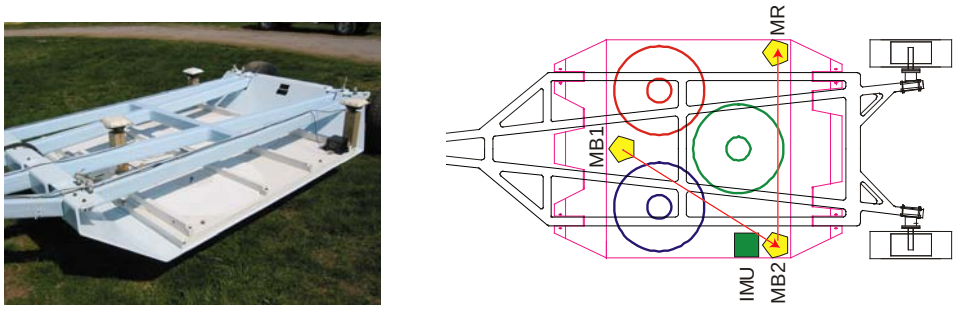

Figure 12. MM-0033 towed GEM-3 array.

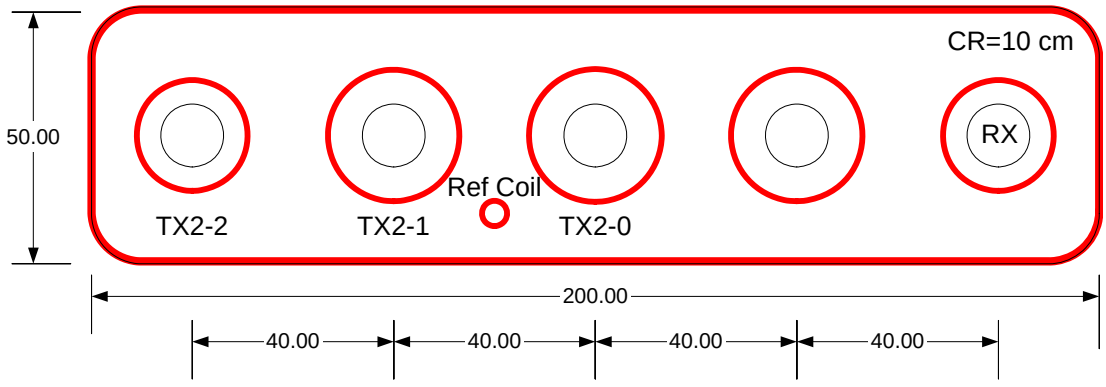

Figure 13. FDEM array configuration for simultaneous magnetometer operation.

4. Sensor Mockup and Bench Testing

Geophex built and tested a working mock-up of a FDEM sensor array and performed test measurements of a set of standard objects verifying the viability of a co-planar FDEM sensor array suitable for co-deployment with standard Cesium vapor magnetometer sensors.

Figure 14 is a photograph of the prototype array as built for this task. The array is made using a half-inch fiberglass-skinned foam board with outer dimensions of 50 cm by 200 cm and with rounded corners. All receiver coils (RX) have the same mean diameter: 12.5 cm. The primary transmitter (TX1) coincides with the board perimeter. The smaller inner transmitters (TX2) provide a magnetic cavity for each RX and have the following diameters, computed rigorously by a numerical integration method:

- TX2-0: Center 26.34 cm
- TX2-1: Off-the-Center 26.10 cm
- TX2-2: Edge 22.02 cm

Table 1 shows electrical details of the TX and RX coils. A small reference coil placed in a magnetically stable location (*cf.* Figure 13) monitors the TX strength as the supply voltage fluctuates and normalizes the RX output, accordingly. At peak current (40 amp) the primary transmit moment is 240 amp-m^2. Output current decreases with frequency, reducing the primary moment to ~100 amp-m^2 at 1 kHz. The loss in the TX moment due to the opposite TX2 (bucking) current is computed to be 7.8%, the price for the magnetic cavity for the all five receiver coils. The peak net transmit moment for the GEM-3's in the MM-0033 array is 33.7 amp-m^2.

Calibration

The receiver coil response in the array, depending on its location, is best characterized by means of a Q-coil that has a known geometry, resistance, and inductance. Specifications for the circular Q-coil used for the calibration of this array are also included in Table 1. The resonant frequency

Figure 14. Laboratory prototype GEM-3 array.

Dave Wright GEM-3 Array August 2006

		1.26E-06	mu0			Constants					
12	supply (volt)	40	current limit (A)	2.00E-09	Rx sensing (V)	384000	TX rate				
TX coil		110	strands								
6	turns	0.003	NE Litz 110	6.00	area x turn (m*m)	1.06E-03	time const (sec)			206.81	wind (mm^2)
2.00	width 2a (m)	9.98E-05	inductance (H)	0.09	resistance (ohm)	0.14	H-bridge IRF1405Z			30.00	length (m)
0.50	width 2b (m)	0.564	equi rad (m)	1.00	a (m)	0.25	b (m)			3.91	winding factor
RX coils											
100	turns	0.3460	AWG#30	1.23	area x turn (m*m)	2.40E-04	time const (sec)			8.43	wind (mm^2)
0.063	rad (m)	3.26E-03	inductance (H)	13.59	resistance (ohm)					39.27	length (m)
0.80	x loc (m)					20.88	h			4.150	winding factor
0.00	y loc (m)	0.32	r1	1.82	r3	7.96	h-up				
0.00	z loc (m)	1.82	r2	0.32	r4	12.92	h-down				
Q-coil											
36.00	turns	4.98E-04	inductance (H)	1.52	resistance (ohm)						
0.081	radius (m)	0.74	area x turn (m*m)	3.775	winding fac (k)						
0.80	x loc (m)					2.78	h				
0.00	y loc (m)	0.59	r1	1.88	r3	0.72	h-up				
0.50	z loc (m)	1.88	r2	0.59	r4	2.07	h-down	1.60E-06	const		

AWG	ohm/m
22	0.0540
24	0.0859
30	0.3460

freq	Q-coil alpha	TX current (Amp)	TX moment (m*m)	Bz primary at RX 1	Bz primary at QX	Current (amp) in QX real	Current (amp) in QX imag	Bz @RX due to QX real	Bz @RX due to QX imag	Q-coil ppm (I)	Q-coil ppm (Q)	unbucked RX out (V)
30	0.062	40.00	240.00	5.01E-04	6.68E-05	3.80E-04	6.14E-03	4.51E-10	7.29E-09	0.9	14.5	0.116
150	0.309	40.00	240.00	5.01E-04	6.68E-05	8.70E-03	2.81E-02	1.03E-08	3.34E-08	20.6	66.6	0.580
210	0.433	40.00	240.00	5.01E-04	6.68E-05	1.57E-02	3.63E-02	1.87E-08	4.31E-08	37.3	86.0	0.812
450	0.928	32.72	196.29	4.10E-04	5.47E-05	3.77E-02	4.06E-02	4.48E-08	4.82E-08	109.2	117.6	1.422
1110	2.290	16.34	98.04	2.05E-04	2.73E-05	3.42E-02	1.49E-02	4.06E-08	1.77E-08	198.1	86.5	1.752
2670	5.507	7.10	42.59	8.89E-05	1.19E-05	1.71E-02	3.11E-03	2.03E-08	3.69E-09	228.4	41.5	1.831
6570	13.552	2.91	17.45	3.64E-05	4.86E-06	7.20E-03	5.31E-04	8.55E-09	6.31E-10	234.6	17.3	1.846
15990	32.982	1.20	7.18	1.50E-05	2.00E-06	2.98E-03	9.02E-05	3.53E-09	1.07E-10	235.7	7.1	1.848
39150	80.752	0.49	2.93	6.12E-06	8.17E-07	1.22E-03	1.51E-05	1.44E-09	1.79E-11	235.9	2.9	1.849
96000	198.014	0.20	1.20	2.50E-06	3.33E-07	4.96E-04	2.51E-06	5.89E-10	2.98E-12	235.9	1.2	1.849

Table 1. Coil parameters for the GEM-3 array prototype.

of the Q-coil ($2\pi f = R/L$) is 486 Hz. The peak quadrature response should occur at this frequency. At low frequencies, the in-phase and quadrature responses should go to zero. At high frequencies the in-phase response should asymptote to a value equal to twice peak quadrature response, while the quadrature response should fall back to zero. Figure 15 shows the measured Q-coil responses for the three TX2 locations. In each case, the Q-coil is placed at a height of 50 cm directly above the receiver coil. The in-phase and quatrature responses are exactly as expected. The differences in the amplitude of the responses at the three locations are due to differences in the net primary field strength at the Q-coil. The relative scaling is purely a function of the array geometry, and in a final implementation correction factors calculated for a nominal target depth could be applied to the data for cosmetic purposes.

Drift

Sensor drift has always been an issue with the GEM-3, especially for the in-phase signal. The standard GEM-3 has concentric coils, which tends to minimize in-phase drift due to thermal expansion of the sensor. Our sensor array lacks the symmetry of the standard GEM-3, and we expect increased drift. The blue curve in Figure 16 shows measured in-phase drift at 2430 kHz for the Tx2-2 location during the initial warmup of our GEM-3 array. The data are very noisy because the testing was done in the laboratory, where lighting, electronic equipment and electrical power all make significant noise contributions. Drift rates at other frequencies and sensor positions are comparable to that seen in Figure 16. These rates are roughly an order of magnitude greater than the corresponding drift rates for the standard GEM-3. In the MM-0033 GEM-3 array, sensor drift is routinely corrected for by applying a 50 sec running median window. The red curve

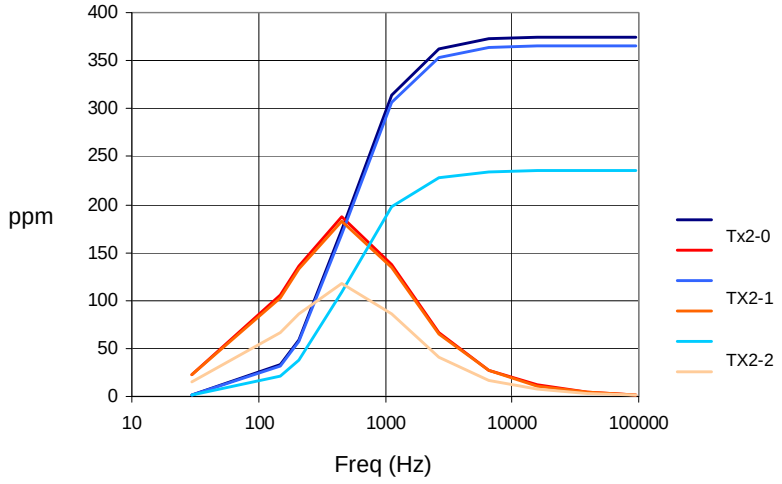

Figure 15. Measured Q-coil responses at three receiver locations.

in Figure 16 shows the effect of applying this filter to our drift data. The drift is effectively reduced to zero.

Array Flexure

Flexure of the array can interfere with primary field nulling at the receive coils. The bucking coils are designed to cancel the net primary field over the area of each receive coil when the array is perfectly planar. Distortion of the main transmit loop distorts its transmitted EM field, resulting in imperfect cancellation by the bucking coils. The effect is illustrated in Figure 17. The sketch on the right shows the geometry. The array is bent between the Tx2+1 and Tx2+2 coils. The plot on the left shows the effect on the primary field contribution from the outer loop at the center of Tx2+1 as a function of the flexure angle θ. The effect becomes quite pronounced for flex angles

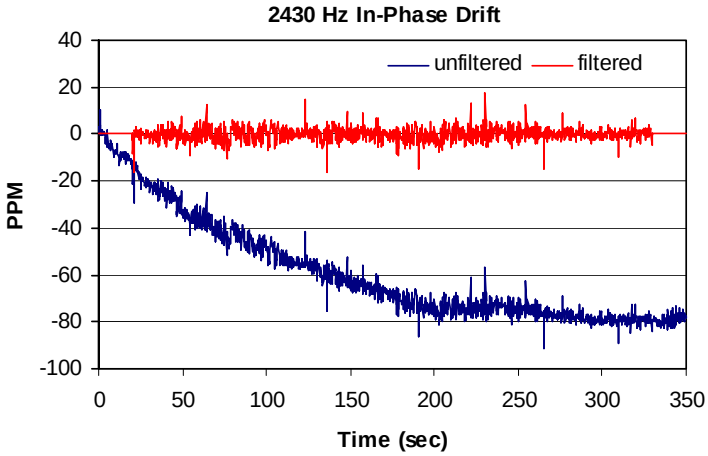

Figure 16. Warmup drift for the GEM-3 array at the Tx2-2 sensor location.

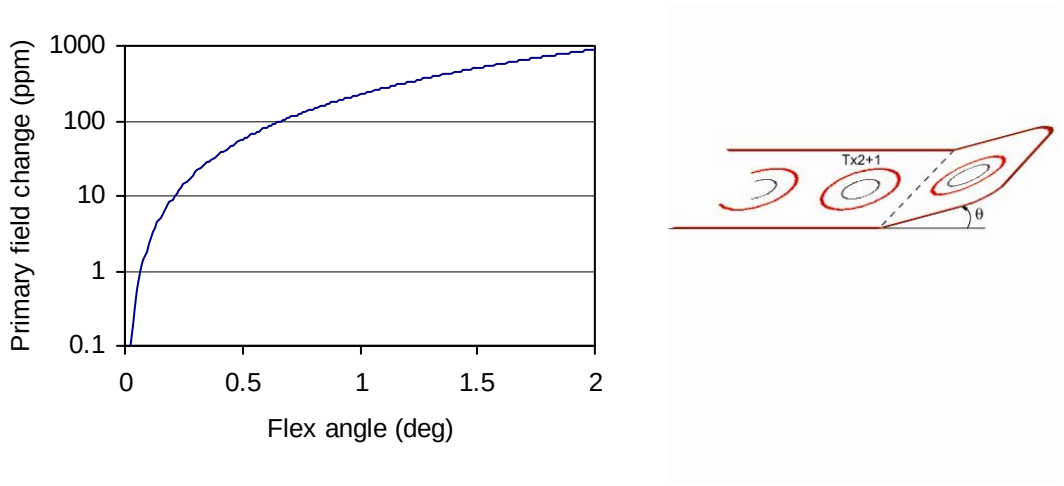

Figure 17. Effect of array flexure on primary field cancellation.

greater than a few tenths of a degree. This is a serious design consideration for the array. One tenth of a degree corresponds to a flexure of about ½ mm over 30 cm. The array would have to be held stiff to this sort of tolerance. For towed applications on land this may be difficult because the array will be subjected to significant bending stresses as it is towed over any realistic terrain. The bouncing and jostling motions for vehicle towed systems tend to have scales comparable to those of buried UXO signals. The situation may not be so serious for marine applications where the array would be buoyed up and not subject to such severe stresses.

Magnetometer Placement

The coil configuration and electrical specifications are suitable for use with Cesium vapor magnetometers, provided that they are positioned at locations where the net transmit field is at a minimum. Figure 18 shows the magnetic field at peak transmit current (7.1 amp at 2.67 kHz) along the long axis of the EM array. Locations of the receive and bucking coils are shown by the blue dots and black squares, respectively. The locations of the ends of the outer transmit coil are shown by the **+** signs. The sensing volume of a Cesium magnetometer is roughly one inch square

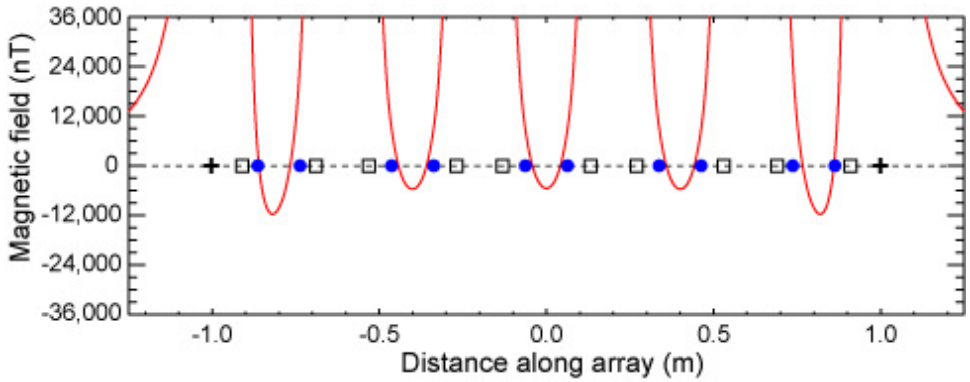

Figure 18. Magnetic field along arrray axis at peak transmit current (2.67 kHz).

(smaller than the blue dots in the figure). Careful placement of the magnetometers near the inside edges of the receive coils, as was done for the handheld EMI/TMF sensor [4], will keep the field strength in the sense volume below a few thousands of nT. Referring back to Figure 3, this should result in EMI induced heading errors of order 10's of nT, which are a bit smaller than those encountered with the EM73/TMF combination shown in Figure 5.

Target Classification and Discrimination

Using EMI data to identify targets and discriminate between UXO and clutter involves inverting the data to estimate the eigenvalues of the target's magnetic polarizability tensor [11]. In order to have enough information to accomplish this, the sensor must interrogate all of the elements of the polarizability tensor, i.e. it must adequately illuminate the target with primary field components in all coordinate directions, and must measure the secondary (induced) field components in all three coordinate directions. Because it relies on a single rectangular transmit coil, the sensor array shown in Figures 13 and 14 will not adequately illuminate targets in the direction parallel to the long axis of the array. Because it has multiple receive coils, the secondary field is adequately sampled. The MM-0033 GEM-3 array provides illumination from all directions because it has multiple transmit coils (although because there are only three elements in the array it generally makes two interleaved passes over the area to provide adequate data density for target classification). This comes at the expense of sequential array element operation and the concomitant switching noise. In order to be effective for discrimination, our array would have to make two surveys over an area in perpendicular directions, as is done with the MTADS EM61 array [12]. That system employs an array of three simultaneously firing EM61 Mark 2 time domain sensors, which act as a single large rectangular transmitter similar to that considered here.

5. Conclusions

The objective of this project was to develop at the proof-of-principle level a multi-frequency, CW frequency-domain EMI sensor array suitable for simultaneous operation with an array of cesium vapor magnetometers. This has been accomplished. The notional array design is shown in Figure 13. A laboratory prototype of the array constructed for this project by Geophex, Ltd. is shown in Figure 14. The design is based on the GEM-3 active primary field cancellation technology, which creates a "magnetic cavity" for each receive coil in the array. The array's magnetometers would be mounted inside the receive coils, within the magnetic cavities. This is very important because the primary transmit field would otherwise be strong enough to shift the total magnetic field vector (static magnetic field plus EMI components) outside the operating envelope of the magnetometers. Because the array configuration does not have the symmetry of a standard GEM-3, in-phase drift tends to be more severe. Tests with the prototype array showed drift rates roughly one order of magnitude larger than with a standard GEM-3. However, demedian filtering such as that used for the MM-0033 towed GEM-3 array can correct for the drift. The most serious issue for our array is structural rigidity. When the array is bent, the bucking coils do not properly cancel the field from the outer transmit loop. Calculations indicate that bucking errors amounting 10's of ppm can be caused by bending the array by a few tenths of a degree over a distance of about 30 cm. The array would have to be held stiff to this sort of tolerance. For towed applications on land this may be difficult because the array will be subjected to significant bending stresses as it is towed over any realistic terrain. The bouncing and jostling motions for vehicle towed systems tend to have scales comparable to those of buried UXO signals. The situation may not be so serious for marine applications where the array would be buoyed up and not subject to such severe stresses.

6. References

1. George Robitaille, Jane Adams, Chris O'Donnell and Pope Burr, "Jefferson Proving Ground Technology Demonstration Program Summary," U. S. Army Environmental Center and Navy Explosive Ordnance Technology Division, Report No. SFIM-AEC-P2/ETD, 24 May 1999.
2. Robert Mark Siegel, Alan L. Crandall and Gilbert Johnson, "Interleaved Magnetometry and Pulsed Electromagnetic Detection of Underground Objects," United States Patent 20050110496, May 26, 2005
3. Rob Siegel and Bob Selfridge, "Man-portable Simultaneous EMI and Magnetometer System (MSEMS)," UXO/Countermine Forum, Las Vegas, July 10-13, 2006.
4. David Wright and Hollis H. (Jay) Bennett Jr., "Simultaneous Deployment of a Total Field Magnetometer and EMI System for UXO," UXO/Countermine Forum, Las Vegas, July 10-13, 2006.
5. David J. Wright and Jim Kingdon, "Development of a Combined EMI/Magnetometer Sensor for UXO Detection," Proc. Symposium on the Applications of Geophysics to Environmental and Engineering Problems (SAGEEP), Colorado Springs, Feb. 22-26, 2004, pp. 1805-1814.
6. I. J. Won, D. A. Keiswetter, D. Hanson, E. Novikova and T. Hall, "GEM-3: A Monostatic Broadband Electromagnetic Induction Sensor," Journal of Environmental and Engineering Geophysics, Vol. 2, No. 1, pp. 53-64, 1997.
7. Bin Le, Thomas W. Rondeau, Jeffrey H. Reed and Charles W. Bostian, "Analog-to-Digital Converters: A Review of the Past, Present and Future," IEEE Signal Processing Magazine, November 2005, pp. 69-77.
8. Sailaja V. Chilaka, Lloyd S. Riggs, Herbert H. Nelson and Thomas H. Bell, "Extremely Low Frequency Response (Below 30 Hz) of UXO-Like Objects," Proc. SPIE Vol. 5415, Detection and Remediation Technologies for Mines and Minelike Targets IX (Russell S. Harmon, J. Thomas Broach and John H. Holloway, Jr., Eds.), pp. 1280-1291, Sept. 2004.
9. Haoping Huang, Bill SanFilipo, Alex Oren and I. J. Won, "Coaxial Electromagnetic Sensor for UXO Detection," Proc. Symposium on the Applications of Geophysics to Environmental and Engineering Problems (SAGEEP), Atlanta, April 3-7, 2005, pp. 1378-1388.
10. B. Barrow, N. Khadr, H. H. Nelson and D. Steinhurst, "Results from a Towed Array of Multiple Frequency EMI Sensors," UXO/Countermine Forum, St. Louis, March 9-12, 2004.
11. Thomas H. Bell, Bruce J. Barrow and Jonathan T. Miller, “Subsurface Discrimination Using Electromagnetic Induction Sensors,” IEEE Transactions on Geoscience and Remote Sensing, Vol. 39, No. 6, June 2001, pp. 1286-1293.
12. Bruce Barrow and H. H. Nelson, "Model-Based Characterization of Electromagnetic Induction Signatures Obtained with the MTADS Electromagnetic Array," IEEE Transactions on Geoscience and Remote Sensing, Vol. 39, No. 6, June 2001, pp. 1279-1285.